Exact-factorization study of the photochemistry of phenol

Audrey Pollien, Evaristo Villaseco Arribas, David Lauvergnat, Federica Agostini

Exact-factorization study of the photochemistry of phenol

Audrey Pollien
Université Paris-Saclay, CNRS, Institut de Chimie Physique UMR8000, 91405, Orsay, France and
Université Paris-Saclay, ENS Paris-Saclay, DER de Chimie, 91190, Gif-sur-Yvette, France
Evaristo Villaseco Arribas
Université Paris-Saclay, CNRS, Institut de Chimie Physique UMR8000, 91405, Orsay, France and
Department of Physics, Rutgers University, Newark 07102, New Jersey, USA
David Lauvergnat
Université Paris-Saclay, CNRS, Institut de Chimie Physique UMR8000, 91405, Orsay, France
Federica Agostini[a)]
Université Paris-Saclay, CNRS, Institut de Chimie Physique UMR8000, 91405, Orsay, France

We present an analysis of the performance of the coupled-trajectory schemes for nonadiabatic dynamics derived from the exact factorization of the electron-nuclear wavefunction and implemented in the G-CTMQC code. These algorithms can be seen as variations of the standard Ehrenfest method and Tully surface hopping, which are based, however, on independent trajectories. The reported analysis aims to compare the coupled-trajectory and the independent-trajectory schemes, and to benchmark the numerical results against exact quantum waavepacket dynamics. To this end, we employ an analyitical molecular model with two nuclear degrees of freedom and three electronic states that allows us to describe the photo-induced hydrogen dissociation in phenol. The analysis focuses on different electronic and nuclear properties calculated along the nonadiabatic dynamics of phenol.

[a)]Electronic mail: federica.agostini@universite-paris-saclay.fr

I. INTRODUCTION

The exact factorization of the time-dependent electron-nuclear wavefunction is a formalism introduced in 2010 by Gross and coworkers[1,2] to express a molecular wavefunction as the product of a marginal nuclear and a conditional electronic amplitude. This formalism is a generalization to the time domain of the analogous static factorization developed by Hunter[3–6] and adopted later on in other groups[7–10], and has found until today many different applications for the interpretation[11–29] and the simulation[30–39] of electron-nuclear dynamics beyond the Born-Oppenheimer approximation.

The exact factorization offers a way to decompose the dynamical problem represented by the molecular time-dependent Schrödinger equation into coupled nuclear and electronic equations for the marginal and for the conditional amplitudes, respectively. The electrons effectively act on the nuclei as time-dependent scalar and vector potentials that completely determine the evolution of the nuclear wavefunction via a nuclear Hamiltonian, thus in the form of a (nuclear) time-dependent Schrödinger equation. These time-dependent potentials incorporate nonadiabatic effects beyond the Born-Oppenheimer approximation[40], and thus involve the ground and excited electronic states which are coupled through the nuclear motion. While only few attempts have been made to solve exactly[41,42] the coupled equations for the marginal and for the conditional amplitudes, the presence of the time-dependent potentials in the nuclear Hamiltonian allows one to easily introduce a picture of the nuclear dynamics in terms of trajectories. Ciccotti and coworkers rigorously reformulated[42,43] the nuclear equation using the method of characteristics, that can be interpreted as quantum trajectories in a Bohmian sense[44], but the main computational advantage has been achieved with a more classical-like treatment of the nuclear dynamics[33,45–47]. Algorithms such as the coupled-trajectory mixed quantum-classical (CTMQC) scheme[45,48–50], along with its energy-conserving variation CTMQC-E[51], and coupled-trajectory Tully surface hopping (CTTSH)[47] allowed us to simulate nonadiabatic processes of various molecular models[36,51,52] and molecular systems using an on-the-fly approach[30,38,53].

CTMQC(-E) and CTTSH describe the nuclear dynamics in terms of an ensemble of coupled classical-like trajectories. These trajectories have to be propagated simultaneously since they reproduce the evolution of an underlying time-dependent nuclear probability density. The classical-like force that guides the trajectories is determined from the time-dependent scalar and vector potentials. The potentials can be expressed in terms of adiabatic energies and nonadiabatic couplings by expanding the time-dependent conditional electronic amplitude in the adiabatic basis, as done in standard procedures for nonadiabatic excited-state dynamics such as Ehrenfest [54] and Tully surface hopping (TSH)[55]. This allows to reconstruct the time-dependent potantials on-the-fly during the dynamics using information provided by standard quantum-chemistry packages. Indeed, the time-dependent state of the electrons is determined by solving the evolution equation for the conditional amplitude along the trajectories ensemble.

We note here that additional simplifications have been introduced by Min and coworkers to propose independent-trajectory algorithms derived from the exact factorization, i.e., the methods surface hopping based on the exact factorization (SHXF) and Ehrenfest dynamics based on the exact factorization (EhXF), allowing one to access complex molecular systems

and processes[33,56–59]. Also, Blumberger and coworkers recently developed CTMQC-(E)DI[60], where a double-intercept (DI) idea is introduced in CTMQC and in CTMQC-E to cure numerical instabilities encountered in these methods when calculating the coupling among the trajectories, thus, greatly improving energy and norm conservation.

Some of these independent and coupled-trajectory algorithms are currently implemented in G-CTQMC package[61]. Therefore, we find interesting at this stage of the computational and theoretical development of the exact factorization, to present an in-depth comparison of the performance of the exact-factorization-based algorithms, namely, CTMQC, CTMQC-E and CTTSH, with Ehrenfest and TSH, using the same molecular example. We choose for this study a three-electronic-state two-nuclear-dimensional molecular model that mimics the hydrogen dissociation in photo-excited phenol[62]. Even though the molecular Hamiltonian is provided as analytical model potentials, the system presents some challenging features, namely (i) the presence of a conical intersection between the bright S_1 state and the dark S_2 state whose access is limited by the initial energy of the photo-excitation, (ii) the presence of two subsequent conical intersections, i.e., S_1/S_2 and S_0/S_1, that are encountered along the ultrafast process that leads to hydrogen dissociation either in S_0 or in S_1, and (iii) the activation of a periodic nuclear variable upon photo-excitation.

Before describing the photo-induced dynamics of phenol, we recall in Section II the exact factorization of the electron-nuclear wavefunction and the coupled-trajectory algorithms that will be used in the numerical analysis. Then, in Section III we describe the molecular model used in the calculations and report our analysis of the dynamics of phenol upon photo-excitation. To finalize, we state our conclusions in Section IV.

II. EXACT FACTORIZATION OF THE MOLECULAR WAVEFUNCTION

The non-relativistic molecular Hamiltonian

$$\hat{H}(\mathbf{r},\mathbf{R}) = \hat{T}(\mathbf{R}) + \hat{H}_{BO}(\mathbf{r},\mathbf{R}) \tag{1}$$

defines a system of interacting electrons and nuclei, whose positions are collectively indicated with the symbols $\mathbf{r}$ and $\mathbf{R}$, respectively. We indicate with $\hat{T}(\mathbf{R})$ the nuclear kinetic energy and with $\hat{H}_{BO}(\mathbf{r},\mathbf{R})$ the sum of remaining terms, i.e., the electronic kinetic energy and all the interactions; $\hat{H}_{BO}(\mathbf{r},\mathbf{R})$ is usually referred to as Born-Oppenheimer (BO) Hamiltonian.

The time-dependent Schrödinger equation (TDSE) with $\hat{H}(\mathbf{r},\mathbf{R})$ dictates the evolution of the molecular wavefunction $\Psi(\mathbf{r},\mathbf{R},t)$ as

$$i\hbar\frac{\partial}{\partial t}\Psi(\mathbf{r},\mathbf{R},t) = \hat{H}(\mathbf{r},\mathbf{R})\Psi(\mathbf{r},\mathbf{R},t) \tag{2}$$

The exact factorization[1,2] states that the total molecular wavefunction can be exactly factorized as a single correlated product

$$\Psi(\mathbf{r},\mathbf{R},t) = \chi(\mathbf{R},t)\Phi(\mathbf{r},t;\mathbf{R}) \tag{3}$$

of a marginal wavefunction, i.e., $\chi(\mathbf{R},t)$, and a conditional amplitude, i.e., $\Phi(\mathbf{r},t;\mathbf{R})$, that parametrically depends on the nuclear coordinates $\mathbf{R}$. The interpretation of $|\Psi(\mathbf{r},\mathbf{R},t)|^2$ as

a joint probability density allows one to easily identify $|\chi(\mathbf{R},t)|^2$ as the marginal probability density of $\mathbf{R}$, with $|\Phi(\mathbf{r},t;\mathbf{R})|^2$ the conditional probability density, whose normalization over $\mathbf{r}$ has to be imposed $\forall\ \mathbf{R},t$. The TDSE combined with such a *partial normalization condition* yields

$$i\hbar\frac{\partial}{\partial t}\chi(\mathbf{R},t)=\left[\sum_{\nu}\frac{[-i\hbar\nabla_{\nu}+\mathbf{A}_{\nu}(\mathbf{R},t)]^2}{2M_{\nu}}+\varepsilon(\mathbf{R},t)\right]\chi(\mathbf{R},t) \tag{4}$$

$$i\hbar\frac{\partial}{\partial t}\Phi(\mathbf{r},t;\mathbf{R})=\left[\hat{H}_{BO}(\mathbf{r},\mathbf{R})+\hat{U}_{en}[\Phi,\chi]-\varepsilon(\mathbf{R},t)\right]\Phi(\mathbf{r},t;\mathbf{R}) \tag{5}$$

which are the coupled evolution equations for $\chi(\mathbf{R},t)$ and $\Phi(\mathbf{r},t;\mathbf{R})$, respectively. The index ν is used to label the nuclei and M_{ν} their masses.

Equation (4) is itself a TDSE where the coupling to the dynamics of $\Phi(\mathbf{r},t;\mathbf{R})$ is expressed in terms of a time-dependent vector potential (TDVP)

$$\mathbf{A}_{\nu}(\mathbf{R},t)=\langle\Phi(t;\mathbf{R})|\ -i\hbar\nabla_{\nu}\Phi(t;\mathbf{R})\rangle_{\mathbf{r}} \tag{6}$$

and a time-dependent potential energy surface (TDPES)

$$\varepsilon(\mathbf{R},t)=\langle\Phi(t;\mathbf{R})|\,\hat{H}_{BO}(\mathbf{r},\mathbf{R})+\hat{U}_{en}[\Phi,\chi]-i\hbar\frac{\partial}{\partial t}\,|\Phi(t;\mathbf{R})\rangle_{\mathbf{r}} \tag{7}$$

In the definitions of the TDVP and TDPES, we indicate with the symbol $\langle\ \cdot\ \rangle_{\mathbf{r}}$ an integration over $\mathbf{r}$, and we use the convention that such variable does not appear explicitly in the term in the bra-ket as it is integrated over.

Note that the product form of the wavefunction $\Psi(\mathbf{r},\mathbf{R},t)$ is invariant under the phase transformations $\tilde{\Phi}(\mathbf{r},t;\mathbf{R})=\exp\left[(i/\hbar)\theta(\mathbf{R},t)\right]\Phi(\mathbf{r},t;\mathbf{R})$ and $\tilde{\chi}(\mathbf{R},t)=\exp\left[(-i/\hbar)\theta(\mathbf{R},t)\right]\chi(\mathbf{R},t)$. Thus, under these transformations, the TDVP and TDPES transform as well, as standard gauge potentials, namely $\tilde{\mathbf{A}}_{\nu}(\mathbf{R},t)=\mathbf{A}_{\nu}(\mathbf{R},t)+\nabla_{\nu}\theta(\mathbf{R},t)$ and $\tilde{\varepsilon}(\mathbf{R},t)=\varepsilon(\mathbf{R},t)+\partial_t\theta(\mathbf{R},t)$, and Eqs. (4) and (5) are form-invariant.

Equation (5) yields the evolution of $\Phi(\mathbf{r},t;\mathbf{R})$, where the coupling to the dynamics of Eq. (4) is provided by the electron-nuclear coupling operator

$$\begin{aligned}\hat{U}_{en}[\Phi,\chi]=&\sum_{\nu}\frac{[-i\hbar\nabla_{\nu}-\mathbf{A}_{\nu}(\mathbf{R},t)]^2}{2M_{\nu}}\\&+\sum_{\nu}\frac{1}{M_{\nu}}\left(\frac{-i\hbar\nabla_{\nu}\chi(\mathbf{R},t)}{\chi(\mathbf{R},t)}+\mathbf{A}_{\nu}(\mathbf{R},t)\right)(-i\hbar\nabla_{\nu}-\mathbf{A}_{\nu}(\mathbf{R},t))\end{aligned} \tag{8}$$

Due to the non-linearity of Eq. (5), the time-evolution of $\Phi(\mathbf{r},t;\mathbf{R})$ does not have a Schrödinger form, unlike the time-evolution of $\chi(\mathbf{R},t)$. As discussed in the Introduction, interesting applications of the exact factorization of the electron-nuclear wavefunction focused on introducing a *trajectory-based perspective* within this framework, such that the nuclear dynamics is ultimately approximated using classical-like trajectories while the electronic dynamics is treated quantum mechanically. The trajectory-based solution of the nuclear equation (4) is introduced naturally, since the classical-like limit simply requires to interpret the TDVP and TDPES as standard (classical) electromagnetic potentials producing a classical force on the nuclei. Therefore, the main efforts in this context have been

devoted to the calculation and approximation of the TDVP and of the TDPES from the solution of the quantum-mechanical electronic equation (5). We describe in Section II A how the concept of classical trajectories is introduced in the exact factorization and recall the approximations leading to the derivation of CTMQC, CTMQC-E and CTTSH.

A. Exact-factorization-based coupled-trajectory algorithms

Accurately and efficiently calculating the electronic TDVP and TDPES in the course of a simulation requires to develop algorithms and software exploiting the strengths of current quantum-chemistry techniques for on-the-fly dynamics. With this idea in mind, let us present and compare the various quantum-classical schemes that have been introduced in recent years to simulate nonadiabatic processes using the exact factorization.

The trajectory-based perspective of the exact factorization requires to replace the concept of a quantum nuclear wavefunction with an ensemble of trajectories. Formally, this is done by replacing $\mathbf{R}$, a $3N_n$-dimensional vector, with N_n the number of nuclei of the system, with the symbol $\mathbf{R}^\alpha(t)$. Here, $\alpha = 1, \ldots, N_{tr}$ labels the trajectories, that have to be many in order to reproduce the delocalization of the nuclei in configuration space. The trajectory-based nuclear dynamics can be simply summarized using Hamilton's equations

$$\dot{\mathbf{R}}_\nu^\alpha(t) = \frac{\mathbf{P}_\nu^\alpha(t)}{M_\nu} \tag{9}$$

$$\dot{\mathbf{P}}_\nu^\alpha(t) = \mathbf{F}_\nu^\alpha(t) \tag{10}$$

where we introduced here, for every trajectory α and for every nucleus ν, the concepts of velocity, i.e., $\dot{\mathbf{R}}_\nu^\alpha(t)$, of (kinematic) momentum, i.e., $\mathbf{P}_\nu^\alpha(t)$, and of force, i.e., $\mathbf{F}_\nu^\alpha(t)$. In particular, $\mathbf{P}_\nu^\alpha(t)$ and $\mathbf{F}_\nu^\alpha(t)$ will be expressed in terms of the TDVP and of the TDPES.

The trajectories can be assimilated to a moving grid: while in the quantum treatment the value of a function $f(\mathbf{R}, t)$ can be determined at time t at any point $\mathbf{R}$, in the trajectory-based treatment only the values $f(\mathbf{R}^\alpha(t), t)$ are accessible. Clearly, for a very large number of trajectories N_{tr}, information is not lost when going from the quantum to the trajectory-based treatment. It is important to note that, in order to evaluate how functions of the type $f(\mathbf{R}^\alpha(t), t)$ evolve, only total time-derivatives can be computed instead of partial time-derivatives.

Aiming to develop on-the-fly procedures to solve the exact-factorization equations, the electronic wavefunction is expanded in the adiabatic basis, i.e., the basis formed by the eigenstates of $\hat{H}_{BO}(\mathbf{r}, \mathbf{R})$. Therefore, the expression $\Phi(\mathbf{r}, t; \mathbf{R}) = \sum_j C_j(\mathbf{R}, t)\varphi_j(\mathbf{r}; \mathbf{R})$ is inserted in Eq. (5) to derive a set of evolution equations for the expansion coefficients $C_j(\mathbf{R}, t)$. Following from the above observations, when the idea of trajectories is introduced, the electronic equation (5) is affected as well, and the evolution of the coefficients is ultimately expressed as a total time-derivative $\dot{C}_j(\mathbf{R}^\alpha(t), t) = \dot{C}_j^\alpha(t)$.

The key quantity arising in such a trajectory-based formulation of the electron-nuclear dynamics is the so-called *quantum momentum*. In Eq. (5), the operator $\hat{U}_{en}[\Phi, \chi]$ depends on the nuclear wavefunction, and, when it is expressed in polar form, i.e., $\chi(\mathbf{R}, t) =$

$e^{iS(\mathbf{R},t)}|\chi(\mathbf{R},t)|$ using its modulus $|\chi(\mathbf{R},t)|$ and phase $S(\mathbf{R},t)$, one gets

$$\begin{aligned}\frac{-i\hbar\nabla_\nu\chi(\mathbf{R},t)}{\chi(\mathbf{R},t)}+\mathbf{A}_\nu(\mathbf{R},t)&=[\nabla_\nu S(\mathbf{R},t)+\mathbf{A}_\nu(\mathbf{R},t)]+i\frac{-\hbar\nabla_\nu|\chi(\mathbf{R},t)|^2}{2|\chi(\mathbf{R},t)|^2}\\&=\mathbf{P}_\nu(\mathbf{R},t)+i\mathbf{Q}_\nu(\mathbf{R},t)\end{aligned}\tag{11}$$

where the term in square brackets is the classical momentum $\mathbf{P}_\nu$, that depends on the TDVP as anticipated above, and it is summed to the quantum momentum $\mathbf{Q}_\nu$, and encodes information about the spatial (de)localization of the nuclear density. The non-local nature of this quantity implies that the exact-factorization trajectory-based schemes require coupling among the trajectories, something which is completely overlooked in independent-trajectory schemes, such as TSH or Ehrenfest.

In deriving CTMQC, the polar form of the nuclear wavefunction is inserted in Eq. (4) and after separating real and imaginary parts two coupled evolution equations result, one for the phase and one for the modulus. As discussed in detail in Refs. [42,43], the equation for the modulus can be completely discarded in the classical limit, i.e., when neglecting the quantum Bohmian potential. The equation for the phase thus become

$$-\frac{\partial}{\partial t}S(\mathbf{R},t)=\sum_\nu\frac{\mathbf{P}_\nu(\mathbf{R},t)^2}{2M_\nu}+\varepsilon(\mathbf{R},t)\tag{12}$$

which is a Hamilton-Jacobi equation that can be solved with the method of characteristics, meaning that this partial differential equation (PDE) is replaced by an infinite set of ordinary differential equations (ODEs) for the characteristics, i.e., the trajectories, along which the PDE is always satisfied. The ODEs have the form given in Eqs. (9) and (10), where, under a specific gauge choice, the force becomes $\mathbf{F}^\alpha_\nu(t)=\dot{\mathbf{A}}^\alpha_\nu(t)$, which yields

$$\begin{aligned}\mathbf{F}^\alpha_\nu(t)=&-\sum_j|C^\alpha_j(t)|^2\nabla_\nu E^\alpha_j-\sum_{j,i}\overline{C}^\alpha_j(t)C^\alpha_i(t)\left(E^\alpha_j-E^\alpha_i\right)\mathbf{d}^\alpha_{\nu,ji}\\&+\sum_j|C^\alpha_j(t)|^2\left(\sum_\mu\frac{2\mathbf{Q}^\alpha_\mu(t)}{\hbar M_\mu}\cdot\mathbf{f}^\alpha_{\mu,j}\right)\left(\mathbf{f}^\alpha_{\nu,j}-\mathbf{A}^\alpha_\nu(t)\right)\end{aligned}\tag{13}$$

We recall that the symbol $C^\alpha_j(t)$ stands for the j-th coefficient in the expansion of the electronic conditional amplitude in the adiabatic basis along the trajectory $\mathbf{R}^\alpha(t)$, and $\overline{C}^\alpha_j(t)$ is its complex conjugate. Furthermore, in the above expression, we introduced the adiabatic energy E^α_j, i.e., the j-th eigenvalue of $\hat{H}_{BO}$, and the nonadiabatic coupling vector $\mathbf{d}^\alpha_{\nu,ji}=\langle\varphi_j(\mathbf{R})|\nabla_\nu\varphi_i(\mathbf{R})\rangle_{\mathbf{r}}|_{\mathbf{R}=\mathbf{R}^\alpha}$, both evaluated at the position $\mathbf{R}^\alpha(t)$. We will define the symbol $\mathbf{f}^\alpha_{\nu,j}$ below.

Determining Eq. (13) requires to calculate the total time-derivative of the TDVP, and, consequently, to express it as in Eq. (6) in terms of the conditional amplitude along a trajectory $\mathbf{R}^\alpha(t)$. To this end, the evolution equations $\dot{C}^\alpha_j(t)$ are needed, namely

$$\dot{C}^\alpha_j(t)=-\frac{i}{\hbar}E^\alpha_jC^\alpha_j(t)-\sum_i\sum_\nu\dot{\mathbf{R}}^\alpha_\nu(t)\cdot\mathbf{d}^\alpha_{\nu,ji}(t)C^\alpha_i(t)+\sum_\nu\frac{\mathbf{Q}^\alpha_\nu(t)}{\hbar M_\nu}(\mathbf{f}^\alpha_{\nu,j}-\mathbf{A}^\alpha_\nu(t))C^\alpha_j(t)\tag{14}$$

The expressions (13) of the classical force and (14) of the evolution of the electronic coefficients define the CTMQC algorithm. The main approximations introduced to derive them are: (i) in the definition of the electron-nuclear coupling operator, Eq. (8), the first term is neglected[63], as well as its contribution in the expression of the TDPES to maintain the gauge invariance; (ii) the spatial variation of the coefficients is expressed in the form $\nabla_\nu C_j^\alpha(t) = \frac{i}{\hbar}\mathbf{f}_{\nu,j}^\alpha C_j^\alpha(t)$, with the force for state j accumulated along the trajectory $\mathbf{f}_{\nu,j}^\alpha = -\int_0^t \nabla_\nu E_j^\alpha d\tau$; (iii) the TDVP along a trajectory, using the expansion of the electronic amplitude in the adiabatic basis in its definition (6), is approximated as $\mathbf{A}_\nu^\alpha(t) = \sum_j |C_j^\alpha(t)|^2 \mathbf{f}_{\nu,j}^\alpha$; (iv) the quantum momentum is approximated by expressing the nuclear density as a sum of frozen Gaussians centered at the positions of the trajectories[30,47].

Note that the CTMQC algorithm, expressed by the equations (13) and (14), can be seen as an Ehrenfest scheme corrected by the coupled-trajectory terms where the quantum momentum appears. Specifically, in both equations, the first two terms are identical to the Ehrenfest scheme. The additional contributions allow one to describe decoherence effects, as it has been extensively discussed in the literature[37,48,64]. Furthermore, the extra term in the electronic evolution equation (14) provides a new mechanism for population transfer mediated by the quantum momentum, that has been shown to be key in accurately capturing multi-state processes such as dynamics through a three-state conical intersection[35,53].

Villaseco Arribas and Maitra pointed out some issues related to the conservation of the classical energy in CTMQC. Therefore, they proposed CTMQC-E[51] by imposing that the classical energy

$$\langle E \rangle = \frac{1}{N_{tr}} \sum_\alpha^{N_{tr}} \left(\sum_\nu^{N_n} \frac{[\mathbf{P}_\nu^\alpha(t)]^2}{2M_\nu} + \sum_j |C_j^\alpha(t)|^2 E_j^\alpha \right) \tag{15}$$

is conserved over the ensemble of coupled trajectories. Note that the second term in parenthesis is the CTMQC expression of the TDPES, following the approximations discussed above. Imposing that the time-derivative of Eq. (15) is zero allows one to define a new accumulated force $\tilde{\mathbf{f}}_{\nu,j}^\beta$ as

$$\tilde{\mathbf{f}}_{\nu,j}^\beta = \frac{\left(-E_j^\beta + \frac{1}{N_{tr}} \sum_\alpha \sum_\nu \mathbf{f}_{\nu,j}^\alpha \cdot \dot{\mathbf{R}}_\nu^\alpha + E_j^\alpha\right)}{\sum_\mu \mathbf{n}_\mu^\beta \cdot \dot{\mathbf{R}}_\mu^\beta} \mathbf{n}_\nu^\beta \tag{16}$$

where $\mathbf{n}_\nu^\beta$ is an arbitrary vector defining the direction of $\tilde{\mathbf{f}}_{\nu,j}^\beta$. While any direction for $\mathbf{n}_\nu^\beta$ in Eq. (16) guarantees energy conservation, we choose $\mathbf{n}_\nu^\beta$ as the instantaneous mechanical momentum of the trajectory $\mathbf{n}_\nu^\beta = M_\nu \dot{\mathbf{R}}_\nu^\beta$, with the reasoning that the accumulated force represents a momentum along the trajectory

$$\tilde{\mathbf{f}}_{\nu,j}^\beta = \frac{\left(-E_j^\beta + \frac{1}{N_{tr}} \sum_\alpha \sum_\nu \mathbf{f}_{\nu,j}^\alpha \cdot \dot{\mathbf{R}}_\nu^\alpha + E_j^\alpha\right)}{2E_{kin}^\beta / M_\nu} \dot{\mathbf{R}}_\nu^\beta \tag{17}$$

with E_{kin}^β the kinetic energy of the trajectory β. The choice of this direction results in the exact-factorization-contribution to the nuclear force in Eq. (13) being parallel to the momentum of the trajectory.

The CTTSH algorithm was proposed with the aim to simultaneously tackle the issue of conservation of the classical energy in CTMQC and simplify the expression of the classical force (13) which requires the expensive calculation of the nonadiabatic coupling vectors. In CTTSH, while the electronic evolution equation is the same as the one used in CTMQC, namely Eq. (14), the trajectories are evolved using adiabatic forces, i.e.

$$\mathbf{F}_{\nu}^{\alpha}(t) = -\nabla_{\nu} E_{active}^{\alpha} \tag{18}$$

where the *active* state is selected stochastically at every time step of dynamics according to the fewest-switches procedure of standard TSH. If during the propagation the active state changes between two time-steps, then the trajectory hops to the new active state, experiencing a change in potential energy which is accompanied by a change in kinetic energy to ensure the classical energy is conserved along the trajectory. Despite the coupled-trajectory nature of CTTSH, energy conservation is imposed at the level of the single trajectory, as done in standard TSH. In the case of a possible hop towards an electronic state higher in (potential) energy, the kinetic energy is expected to decrease. However, if a trajectory does not have sufficient kinetic energy to offset the extra potential energy gained during the hop, the hop is frustrated and does not take place. Note that in TSH, the electronic evolution equation is identical as the one in Ehrenfest, thus it is given by the first two terms of Eq. (14). As observed for CTMQC, the additional coupled-trajectory contribution that depends on the quantum momentum in Eq. (14) induces decoherence effects in CTTSH as well. Instead, to achieve decoherence in a standard TSH procedure, the original algorithm needs to be modified using decoherence corrections, as we will do in Section III employing the widely used energy-based decoherence (ED) correction of Ref. [65].

All the algorithms illustrated so far are currently implemented in the G-CTMQC package[61] and can be freely accessed on GitLab under GNU Lesser General Public License (LGPL).

III. TRAJECTORY-BASED STUDIES OF PHOTO-EXCITED PHENOL

In this section, we aim to discuss the strengths and weaknesses of the coupled-trajectory algorithms derived from the exact factorization. We test these schemes against the independent-trajectory methods Ehrenfest and TSH, using exact quantum-dynamics results to benchmark the trajectory simulations. All calculations are performed using the same model Hamiltonian, and all trajectory-based simulations are carried out with G-CTMQC.

We simulated the photo-induced hydrogen dissociation reaction in phenol[66–71] employing the two-nuclear-dimensional model Hamiltonian including three electronic states proposed in Ref. [62]. To the best of our knowledge, this particular model of phenol has not been previously used in the literature to carry out an extensive comparison of trajectory-based methodologies, as we will present here. Despite its simplicity, the model presents some interesting features that makes it challenging for approximate methods, such as the use of periodic boundary conditions or the presence of multiple conical intersections that are encountered consecutively and give rise to recrossings.

We performed simulations using the G-CTMQC code[61] which is interfaced with the model potentials library QuantumModelLib[72], where the used phenol model has been implemented.

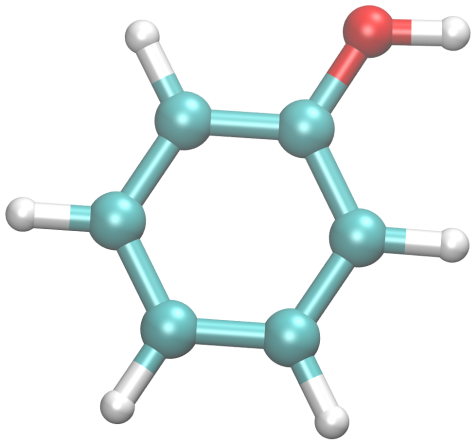

Fig. 1. Ball-and-stick representation of the phenol molecule.

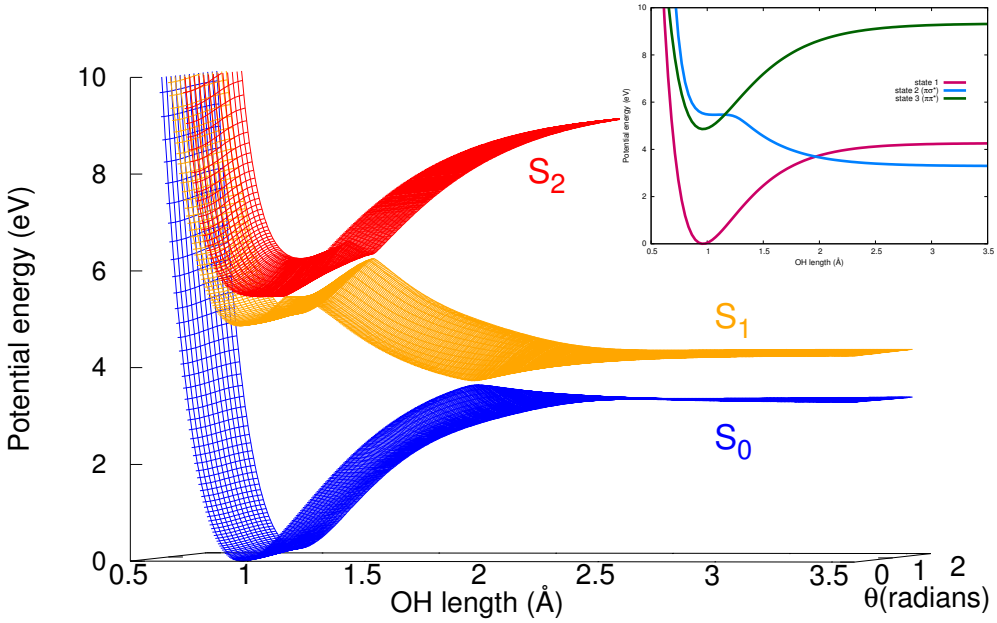

Fig. 2. Adiabatic PESs for the ground state S_0 (in blue), first excited state S_1 (in orange) and second excited state S_2 (in red), as function of the active nuclear coordinates r and θ. Inset: Diabatic potentials represented by the functions $V_{11}(r, \theta = 0)$ (red-violet line), $V_{22}(r, \theta = 0)$ (light-blue line) and $V_{33}(r, \theta = 0)$ (green line).

We tested CTMQC, CTTSH and CTMQC-E, and we report on the comparison with Ehrenfest dynamics and TSH using energy-based decoherence correction (TSHED). Benchmark results are provided by the numerically exact solution of the TDSE by propagating vibronic wavepackets using the ElVibRot code[73].

Information about the model used in our simulations is given in Appendix A. The three electronic states, the ground and the two excited singlet states will be indicated as S_0, S_1, and S_2 respectively. A ball-and-stick representation of phenol is shown in Fig. 1 and the adiabatic

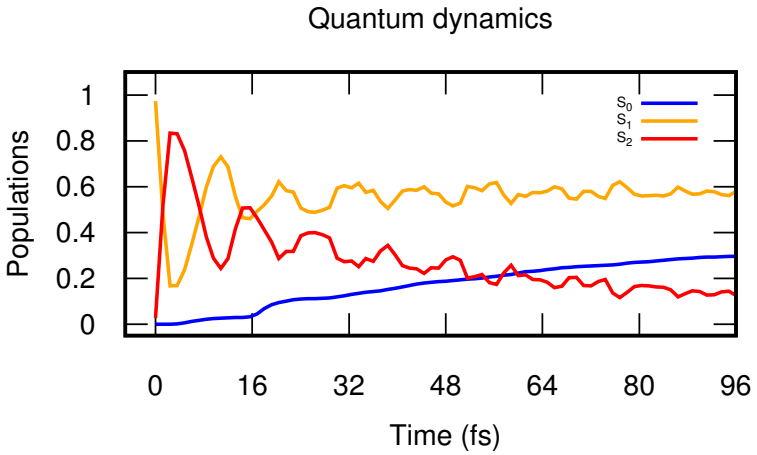

Fig. 3. Populations of the electronic states as functions of time calculated based on the quantum dynamics simulation. In blue we show the population of the ground state S_0, in orange that of the first excited state S_1 and in red that of the second excited state S_2.

potential energy surfaces (PESs) are represented in Fig. 2 as functions of the OH bond length r and of the angle θ formed by the OH bond with the plane of the cycle. The figure shows that S_0 and S_1 have a dissociative character for large values of r, thus hydrogen dissociation takes place either in the ground state or in the first excited state. The photochemistry of phenol is activated by exciting the molecule from the ground state S_0 (blue surface) to the bright state S_1 (orange surface), since in the Franck-Condon region, i.e., around the minimum of S_0 where the photo-excitation process starts, the S_1 state has a $\pi\pi^*$ character. The inset in Fig. 2 shows, using a cut of the PESs at $\theta = 0$, the diabatic potential curves (PECs) with the states labelled as in Appendix A. The diabatic PECs clearly show that the minimum of the bright $\pi\pi^*$ state (green curve) almost coincides with the minimum of the ground state (red-violet curve) and that the closest degeneracy point (conical intersection between S_1 and S_2) between the $\pi\pi^*$ state and the $\pi\sigma^*$ state (dark state, turquoise curve) is higher in energy than the value of the $\pi\pi^*$ energy at the Franck-Condon point, i.e., the minimum of the ground state. This means that upon photo-excitation of the vibrational ground state from S_0 to S_1, the hydrogen dissociation cannot be activated (not even considering the zero point energy): if the dark state $\pi\sigma^*$ is not populated, then the system cannot reach the dissociative regions of the potentials and remains trapped in the minimum of the $\pi\pi^*$ state. In Ref. [62], in fact, an excited vibrational state of S_0 was promoted to S_1 in order to activate the photochemical reaction. Due to the difficulties in creating a vibrational excited state using a classical distribution of trajectories, we opted in our simulations to provide the necessary energy to reach the conical intersection by adding an additional momentum p_0 in the r direction. Indeed, the quantum dynamics results used as benchmark here are obtained in the same conditions. Computational details are provided in Appendix B.

Figure 3 shows the electronic state populations as functions of time obtained with quantum dynamics. As we can observe, after an initial wavepacket excitation from S_0 to S_1 with sufficient kinetic energy to reach the S_1/S_2 conical intersection, the S_2 state gets rapidly populated within the first few femtoseconds. Some population remains in S_1, either because it does not have enough energy to reach S_2 or because it is able to overcome the S_1 energy

barrier towards the dissociative path. In S_2, one portion of the photo-excited wavepacket goes back towards the S_1 minimum and we observe a decrease in the S_2 population (red curve) which reaches a minimum at around 10 fs. At the same time, another portion of the S_2 wavepacket funnels down S_1 and access the dissociative region. We observe a slow rise of the ground state population (blue curve) from around 16 fs, which indicates that the S_1 wavepacket reaches the second conical intersection S_0/S_1. As the dynamics proceeds, the population of S_1 stabilizes towards 0.6, suggesting that the corresponding wavepacket either remains trapped at the minimum of S_1 or is moving in the dissociative portion of the PES; at the same time, the population of S_0 increases and that of S_2 decreases.

The left pannel of Figure 4 compares the trajectory-averaged electronic state populations obtained with CTMQC, CTMQC-E, CTTSH, Ehrenfest and TSHED with the corresponding quantum-dynamics benchmark. Let us first focus on the surface-hopping-based schemes, TSHED and CTTSH. At short times, these methods do not correctly capture the oscillations in the S_1 and S_2 populations, due to the well-known problem of frustrated hops. Essentially, since this short-time dynamics implies electronic transitions from a low-lying state to a high-lying state, some trajectories do not have enough kinetic energy to compensate for the increase of potential energy, and conserve total energy. Conversely, Ehrenfest shows very good agreement with the quantum dynamics results at short times but deviates from the reference after 16 fs. On the other hand, CTMQC and CTMQC-E are able to capture the oscillations in the electronic populations within the first 16 fs of the dynamics, with CTMQC-E in much better agreement with the reference than CTMQC and Ehrenfest. At long times, CTMQC predicts the populations of the electronic states in quite good agreement with the reference and slightly better than CTMQC-E, even though it misses the oscillations in the populations of S_1 and S_2. Interestingly, CTMQC-E predicts population transfer from the ground S_0 state to the S_1 state at 48 fs. CTTSH slightly overestimates the population of the ground state all along the dynamics, and in general it shows a behavior similar to TSHED. Note that for CTTSH we show as continuous lines the trajectory-averaged electronic populations, i.e $\sum_\alpha |C_j^\alpha(t)|^2/N_{tr}$ (with $j = S_0$, S_1 or S_2) and with dashed lines the fraction of trajectories whose dynamics is driven by the corresponding (active) PES. The discrepancy between the two estimates of the populations in CTTSH, could be likely attributed to the ocurrence of frustrated hops. Therefore, current studies on CTTSH are directed towards curing the issue of frustrated hops exploiting the coupled-trajectory nature of the algorithm. Note also that the issue of frustrated hops has been recently addressed by Maitra and coworkers in the independent-trajectory quantum trajectory surface hopping method based on the exact factorization (QTSH-XF)[74].

Figure 4 (right) shows the trajectory-based indicator of coherence between the states S_0/S_1 (top panel), S_1/S_2 (middle panel) and S_0/S_2 (bottom panel) as function of time, as well as the quantum-mechanical analogous quantity scaled down two and three times, respectively, to superimpose the plots to the trajectory-based results. It is not surprising that quantitative agreement with the reference is missing throughout the trajectory-based results, which is probably consequence of the disagreement in the predictions of the electronic populations (see Appendix B for the relation between the indicator of coherence and the populations). The S_0/S_1 indicator represented in black in the top right panel of Fig. 4 increases without reaching a plateau within the simulated time, which is due to the fact that

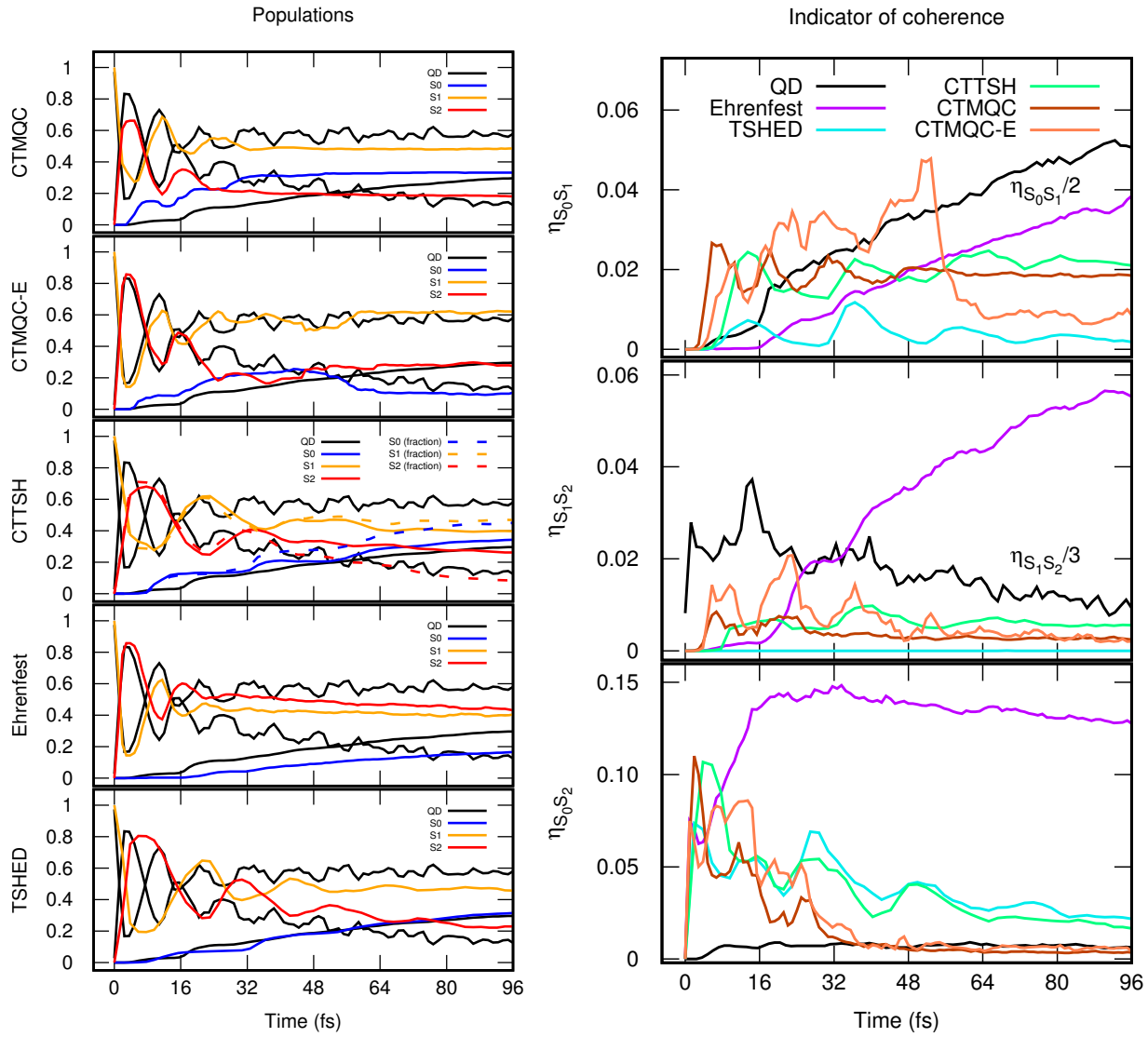

Fig. 4. Left: Populations of the electronic states as functions of time. In black (QD), results of the quantum dynamics are shown, and in color the trajectory-based results: blue for the ground state, orange for the first excited state and red for the second excited state. From top to bottom we show: CTMQC, CTMQC-E, CTTSH, Ehrenfest, TSHED. Right: Indicator of coherence as function of time between the states S_0 and S_1 (top panel), between the states S_1 and S_2 (middle panel) and between the states S_0 and S_2 (bottom panel). In black (QD), the results of exact calculations are shown, in magenta Ehrenfest, in cyan TSHED, in green CTTSH, in brown CTMQC and in orange CTMQC-E.

the ground state population keeps increasing in the region where the S_0 and S_1 wavepackets overlap. Therefore, only Ehrenfest is able to capture qualitatively this coherent behavior, where the other methodologies induce a fictitious decoherence behavior, which is the largest in TSHED and CTMQC-E (at least towards the end of the simulation). We observe also that the decrease of the ground state population observed in CTMQC-E at 48 fs is also reflected in a decrease in the electronic coherences. The exact S_1/S_2 indicator (black curve in the middle right panel of Fig. 4) is non-zero already at the initial time, proving that the state S_1 transfers population to S_2 since the beginning of the simulated dynamics. The offset for

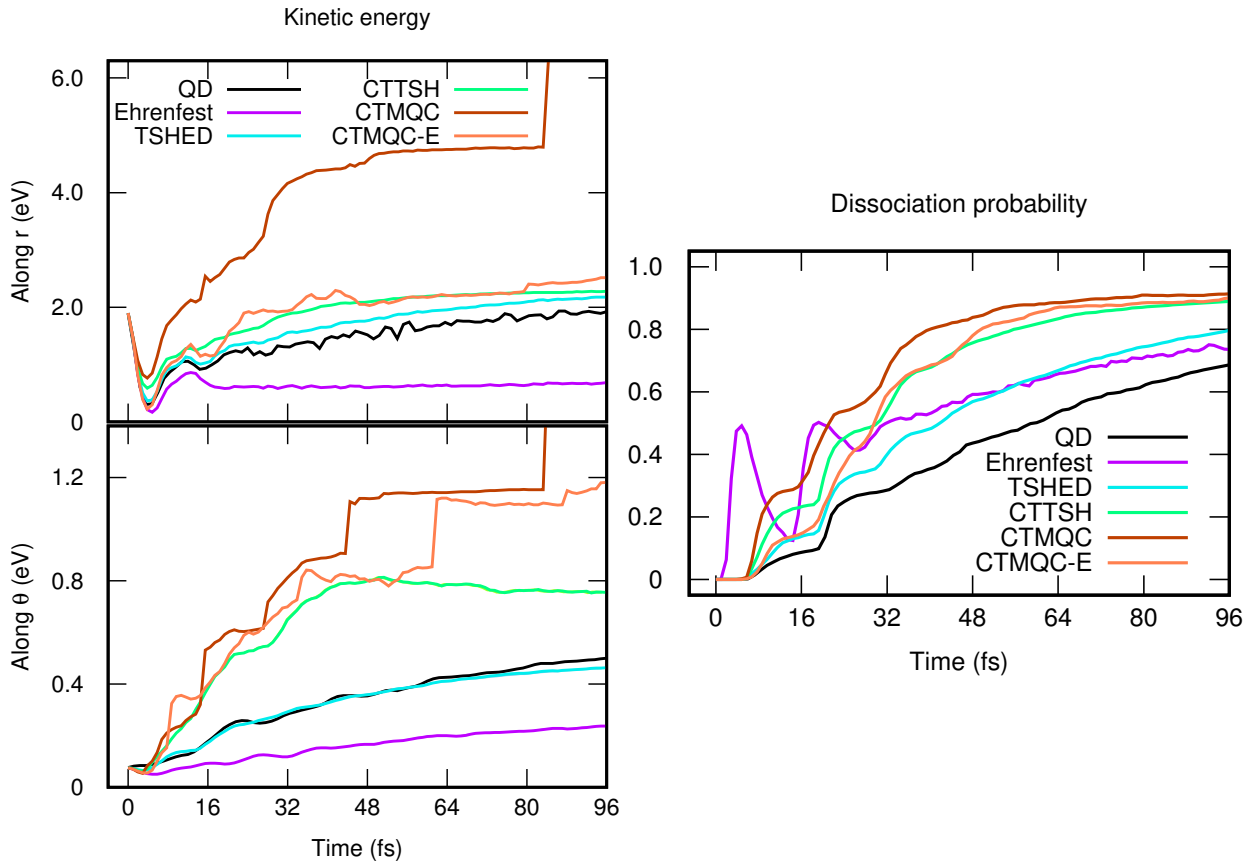

Fig. 5. Left: Nuclear kinetic energy as function of time along the nuclear coordinate r (upper panel) and θ (lower panel). Right: Dissociation probabilities as functions of time. The color code is the same as in Fig. 4 (right).

the transfer is delayed in the trajectory-based calculations, but the increase of the indicator (colored curves in the middle right panel of Fig. 4) takes place in the first few femtoseconds of dynamics. Even though quantitative agreement is missing, the S_1/S_2 indicator remains more or less constant during the dynamics with large oscillations at the beginning. This behavior is qualitatively captured only by the coupled-trajectory methods. In the case of the S_0/S_2 indicator shown in the bottom panel on the right of Fig. 4, quantitative agreement between CTMQC(-E) and exact results is achieved at long times, with Ehrenfest remaining overcoherent all along the dynamics (as for S_1/S_2).

Figure 5 (left) reports the nuclear kinetic energy along the two nuclear directions r (upper panel) and θ (lower panel) as function of time. We observe that the nuclear kinetic energy in Ehrenfest is too small compared to the reference along both coordinates, which is probably due to the fact that the potential energy is overestimated already after about 35 fs. Specifically, in Ehrenfest the potential energy is the average of the electronic adiabatic energies weighted by the populations. Then, since in particular the population of S_1 is overestimated at the expenses of S_0, it is not surprising that the kinetic energy is small (in Ehrenfest the classical total energy is conserved along each trajectory). TSHED does indeed a good job in reproducing the exact kinetic energy, while CTTSH overestimates the kinetic energy along

both directions. In CTTSH, this happens for the opposite reason if compared to Ehrenfest, as in CTTSH the ground state population is overestimated at the expenses of S_1. Instabilities in the nuclear kinetic energy can be observed in CTMQC, which are slightly kept under control in CTMQC-E.

Figure 5 (right) shows the dissociation probability as function of time, namely the amount of density/trajectories that reach and evolve beyond the cutoff distance chosen as $r_{\mathrm{cutoff}} = 2.6$ Å. In general, all trajectory-based methods overestimate the dissociation probability since the initial times. The strong oscillations predicted by Ehrenfest at the beginning of the simulation do not appear in the reference results. Specifically, the black curve in the right panel of Fig. 5 shows clear steps up to about 32 fs, which are quite well reproduced, at least qualitatively, by the other trajectory-based methods. At long times the coupled trajectory methods agree among themselves, but yield higher probability than TSHED and quantum results.

IV. CONCLUSIONS

In this work, we reported on a comparison between the coupled-trajectory schemes for nonadiabatic dynamics derived from the exact factorization and implemented in G-CTMQC, namely CTMQC, CTMQC-E and CTTSH, and the corresponding independent-trajectory methods Ehrenfest and surface hopping. We chose to perform the calculations on a molecular model for the photo-induced hydrogen dissociation process in phenol that despite its simplicity (analytical model with three electronic states and two nuclear coordinates) presents some fundamental challenges for the methods above, as we illustrated in the numerical studies reported here. The trajectory-based results have been benchmarked against exact results obtained based on the propagation of quantum vibronic wavepackets.

Based on the analysis of various properties, namely electronic populations and coherences, nuclear kinetic energy and dissociation probability, we conclude that there is not a unique coupled-trajectory method that stands out for its agreement with the reference results. CTMQC and CTMQC-E perform well in general, but the kinetic energy in CTMQC shows some instabilities that are somehow reduced by the energy-conserving correction of CTMQC-E. The hydrogen dissociation probability at long times is overestimated by all coupled-trajectory methods, but this is not surprising since the populations of the electronic states with dissociative character, namely S_0 and S_1, is not in perfect agreement with exact calculations.

It is interesting to note that the energy-conserving correction in CTMQC-E improves on the performance of CTMQC. In addition, the poor performance of CTTSH is probably due to the incorrect prediction at very short times of the population exchange between S_1 and S_2. This disagreement of CTTSH with the reference has been ascribed to the problem of frustrated hops, affecting equally CTTSH and surface hopping. Therefore, further studies will be focused on treating the problem of frustrated hops in CTTSH reformulating energy conservation and the hopping probability in a way that is more adequate to the coupled-trajectory nature of CTTSH than the current implementation.

ACKNOWLEDGEMENTS

This work was supported by the ANR Q-DeLight project, Grant No. ANR-20-CE29-0014 of the French Agence Nationale de la Recherche and by the Chateaubriand Fellowship from the Mission Scientifique et Technologique of the Embassy of France in the United States.

Appendix A: Phenol model

The electronic Hamiltonian in the diabatic basis is[62]

$$\hat{H}_{BO}(r,\theta) = \begin{pmatrix} V_{11} & V_{12} & V_{13} \\ V_{12} & V_{22} & V_{23} \\ V_{13} & V_{23} & V_{33} \end{pmatrix} \tag{A1}$$

with the state 1 being the ground state in the Franck Condon region, the state 2 having a $\pi\sigma^*$ character and state 3 having a $\pi\pi^*$ character. The electronic Hamiltonian depends on the nuclear coordinates r and θ, which are the only two "active" modes used in the model, and stand for the OH distance and the CCOH dihedral angle, respectively.

The diagonal elements of the electronic Hamiltonian are the diabatic potentials, shown in the inset of Fig. 2 as functions of r for $\theta = 0$. The diagonal elements depend on r and θ as follows

$$V_{11}(r,\theta) = v_{10}(r) + v_{11}(r)\,[1-\cos(2\theta)] \tag{A2}$$

$$V_{22}(r,\theta) = v_{20}(r) + v_{21}(r)\,[1-\cos(2\theta)] + v_{22}(r)\,[1-\cos(2\theta)]^2 \tag{A3}$$

$$V_{33}(r,\theta) = v_{30}(r) + v_{31}(r)\,[1-\cos(2\theta)] \tag{A4}$$

The functions of r in these expressions are

$$v_{10}(r) = D_e^1 \left[1 - \exp\left(-a_1(r - r_1)\right)\right]^2 \tag{A5}$$

$$v_{11}(r) = \frac{1}{2} A_1 \left[1 - \tanh\left(\frac{r - A_2}{A_3}\right)\right] \tag{A6}$$

$$v_{20}(r) = \frac{1}{2}\left[v_{201}(r) + v_{202}(r)\right] - \frac{1}{2}\sqrt{\left(v_{201}(r) - v_{202}(r)\right)^2 + \chi_{20}} \tag{A7}$$

$$v_{21}(r) = \frac{1}{2}\left[v_{211}(r) + v_{212}(r)\right] + \frac{1}{2}\sqrt{\left(v_{211}(r) - v_{212}(r)\right)^2 + \chi_{21}} \tag{A8}$$

$$v_{22}(r) = \frac{1}{2}\left[v_{221}(r) + v_{222}(r)\right] - \frac{1}{2}\sqrt{\left(v_{221}(r) - v_{222}(r)\right)^2 + \chi_{22}} \tag{A9}$$

$$v_{30}(r) = D_e^3 \left[1 - \exp\left(-a_3(r - r_3)\right)\right]^2 + a_{30} \tag{A10}$$

$$v_{31}(r) = \frac{1}{2} C_1 \left[1 - \tanh\left(\frac{r - C_2}{C_3}\right)\right] \tag{A11}$$

$$\tag{A12}$$

with

$$v_{201}(r) = B_{201} \left[1 - \exp\left(-B_{202}(r - B_{203})\right)\right]^2 + B_{204} \tag{A13}$$

$$v_{202}(r) = B_{205} \exp\left(-B_{206}(r - B_{207})\right) + B_{208} \tag{A14}$$

$$v_{211}(r) = \frac{1}{2} B_{211} \left[1 - \tanh\left(\frac{r - B_{212}}{B_{213}}\right)\right] \tag{A15}$$

$$v_{212}(r) = \frac{1}{2} B_{214} \left[1 - \tanh\left(\frac{r - B_{215}}{B_{216}}\right)\right] + B_{217} \tag{A16}$$

$$v_{221}(r) = \frac{1}{2} B_{221} \left[1 + \tanh\left(\frac{r - B_{222}}{B_{223}}\right)\right] \tag{A17}$$

$$v_{222}(r) = \frac{1}{2} B_{224} \left[1 - \tanh\left(\frac{r - B_{225}}{B_{226}}\right)\right] \tag{A18}$$

The off-diagonal elements of the electronic Hamiltonian are

$$V_{12}(r, \theta) = \lambda_{12}(r) \sin(\theta) \tag{A19}$$

$$V_{23}(r, \theta) = \lambda_{23}(r) \sin(\theta) \tag{A20}$$

$$V_{13}(r, \theta) = 0 \tag{A21}$$

with

$$\lambda_{12}(r) = \frac{1}{2} \lambda_{12,max} \left[1 - \tanh\left(\frac{r - d_{12}}{\beta_{12}}\right)\right] \tag{A22}$$

$$\lambda_{23}(r) = \frac{1}{2} \lambda_{23,max} \left[1 - \tanh\left(\frac{r - d_{23}}{\beta_{23}}\right)\right] \tag{A23}$$

The nuclear kinetic energy is given as[62]

$$\hat{T}_n = \hat{T}_{n,r} + \hat{T}_{n,\theta} \tag{A24}$$

$$= -\frac{\hbar^2}{2\mu_{\mathrm{OH}}}\frac{\partial^2}{\partial r^2} - \frac{\hbar^2}{2I}\frac{\partial^2}{\partial \theta^2} \tag{A25}$$

where μ_{OH} is the OH reduced mass and I is the moment of inertia

$$\frac{1}{I} = \frac{1}{I_1} + \frac{1}{I_2} \tag{A26}$$

with

$$I_1 = \mu_{\mathrm{OH}} \left(r_1 \sin\alpha\right)^2 \tag{A27}$$

$$I_2 = 4m_C \left(r_{\mathrm{CC}} \sin\frac{\pi}{3}\right)^2 + 4m_H \left((r_{\mathrm{CH}} + r_{\mathrm{CC}}) \sin\frac{\pi}{3}\right)^2 \tag{A28}$$

Note that in the original model of Ref. [62], I_1 was a function of r. However, in our calculations, we used the constant value of I_1 at r_1, i.e., at the equilibrium OH distance of the electronic ground state. In the above expressions, α is the COH angle, r_{CC} is the CC distance and r_{CH} is the CH distance at the equilibrium ground state geometry. All the parameters of the model are listed in Table 1; the reported values of α, r_{CC} and r_{CH} have been determined by optimizing the phenol molecule using density functional theory at the B3LYP/6-311G(d,p) level of theory with Gaussian16[75].

Diagonalization of the electronic Hamiltonian (A1) yields the adiabatic PESs, shown in Fig. 2. The PESs and corresponding adiabatic states are labelled S_0 (blue surface), S_1 (orange surface) and S_2 (red surface), and present two conical intersections that are clearly identified in Fig. 2.

Appendix B: Computational details

Using the model Hamiltonian just documented, we studied the coupled electron-nuclear dynamics initiated upon a $\pi\pi^*$ excitation. A vibrational wavepacket of the form

$$\chi(r,\theta,0) = \sqrt[4]{\frac{1}{\pi\sigma_r^2}}\, e^{-\frac{(r-r_0)^2}{2\sigma_r^2}} \sqrt[4]{\frac{1}{\pi\sigma_\theta^2}}\, e^{-\frac{\theta^2}{2\sigma_\theta^2}}\, e^{\frac{i}{\hbar}p_0 r} \tag{B1}$$

is prepared at time $t = 0$ in S_0, with $r_0 = r_1$, $p_0 = 28\ \hbar$ Å^{-1} (15 a.u.), $\sigma_r = 0.092$ Å and $\sigma_\theta = 0.55$ rad. The wavepacket is then excited instantaneously to S_1.

We performed calculations with non-zero initial momentum in the r-direction such that the initial nuclear wavepacket has enough energy to access the first conical intersection between S_1 and S_2. In Ref. [62], the system was initially excited electronically in S_1 *and* vibrationally, in order to provide the necessary energy to achieve hydrogen dissociation; in our work, we provide such energy by "kicking" the initial wavepacket centered at r_1.

The quantum dynamics calculations were performed using the short iterative Lanczos scheme[76,77] for a propagation time of 4000 a.t.u. (about 96 fs) with a time step of 50

Parameter	Value	Parameter	Value
D_e^1	4.26302 eV	D_e^3	4.47382 eV
a_1	2.66021 Å^{-1}	a_3	2.38671 Å^{-1}
r_1	0.96944 Å	r_3	0.96304 Å
		a_{30}	4.85842 eV
A_1	0.27037 eV	C_1	0.110336 eV
A_2	1.96606 Å	C_2	1.21724 Å
A_3	0.685264 Å	C_3	0.06778 Å
B_{201}	0.192205 eV	$\lambda_{12,max}$	1.47613 eV
B_{202}	5.67356 Å^{-1}	d_{12}	1.96984 Å
B_{203}	1.03171 Å	β_{12}	0.494373 Å
B_{204}	5.50696 eV	$\lambda_{23,max}$	0.327204 eV
B_{205}	4.70601 eV	d_{23}	1.22594 Å
B_{206}	2.49826 Å^{-1}	β_{23}	0.0700604 Å
B_{207}	0.988188 Å		
B_{208}	3.3257 eV	r_{CC}	1.39403 Å
χ_{20}	0.326432 eV^2	r_{CH}	1.08441 Å
B_{211}	-0.2902 eV	α	109.1333°
B_{212}	2.05715 Å		
B_{213}	1.01574 Å	μ_{OH}	1.57456·10^{-27} kg
B_{214}	-73.329 eV		
B_{215}	1.48285 Å		
B_{216}	-0.1111 Å		
B_{217}	-0.00055 eV		
χ_{21}	0.021105 eV^2		
B_{221}	27.3756 eV		
B_{222}	1.66881 Å		
B_{223}	0.20557 Å		
B_{224}	0.35567 eV		
B_{225}	1.43492 Å		
B_{226}	0.56968 Å		
χ_{22}	0.00 eV^2		

Table 1. List of the parameters of the model Hamiltonian.

a.t.u. (about 1.2 fs). In this Lanczos procedure, the Krylov space is expanded until the norm of a new vector is less than 10^{-10}. The wavepacket is represented in the diabatic representation, and in each electronic state the wavepacket is expanded in a two-dimensional direct product grid or basis set. The primitive basis sets associated with the angle θ and with the r distance are a real Fourier series (64 basis functions) and a particle-in-a-box in the range [0.5, 60] bohr with 2048 basis functions, respectively. This very large range along r is needed to avoid reflection before the end of the propagation time. Since the quantum dynamics is performed in the diabatic representation, the corresponding initial wavepacket is slightly different from the adiabatic one used for the trajectories. In the diabatic representation, the initial wavepacket is given by Eq. (B1) in the third diabatic state, which corresponds to a population in S_1 of more than 97% instead of the 100% for the trajectories.

The calculations were performed with the ELVIBROT Fortran code[73].

Trajectory-based calculations were performed using the G-CTMQC code.[61] For Ehrenfest, CTMQC and CTMQC-E, we run $N_{traj} = 1000$ trajectories, whereas for TSHED and CTTSH, we repeated $n = 5$ times the calculations with $N_{traj} = 1000$ trajectories to sample over various hopping histories. The same initial conditions, i.e., positions and momenta, were used in all calculations, by sampling them from the harmonic Wigner distribution obtained from $|\chi(r, \theta, 0)|^2$ of Eq. (B1). G-CTMQC uses the velocity-Verlet algorithm and the Runge-Kutta-Gill scheme to integrate the nuclear and electronic evolution equations, respectively. The trajectories were propagated for 96 fs (4000 a.t.u.) using a time step of $dt_n = dt_e = 0.0012$ fs (0.05 a.t.u.) for both nuclear dt_n and electronic dt_e dynamics; however, tests were performed by changing the nuclear and the electronic time steps, to $dt_n = dt_e = 0.0024$ fs and to $dt_n = 0.0024$ fs, $dt_e = 0.0012$ fs, to assess the stability of the results.

In Section III, we discuss the performance of the trajectory-based methods in comparison to quantum – exact – results, based on various electronic and nuclear observables. We will show the electronic populations,

$$\rho_{\mathrm{S}_I}(t) = \int dr \int d\theta \, |\chi_{\mathrm{S}_I}(r, \theta, t)|^2 \quad \text{with } I = 0, 1, 2 \tag{B2}$$

the nuclear kinetic energy along the two active coordinates,

$$T_{n,r/\theta}(t) = \int dr \int d\theta \, \langle \Psi(r, \theta, t)| \, \hat{T}_{n,r/\theta} \, |\Psi(r, \theta, t)\rangle \tag{B3}$$

and the dissociation probability,

$$P^{diss}(t) = \int_{r_{\mathrm{cutoff}}}^{+\infty} dr \int d\theta \, |\chi(r, \theta, t)|^2 \tag{B4}$$

with $r_{\mathrm{cutoff}} = 2.6$ Å, as functions of time. Here, we indicate the total nuclear probability density as $|\chi(r, \theta, t)|^2$, that can be obtained as a sum over the three electronic contributions

$$|\chi(r, \theta, t)|^2 = \sum_{I=0,1,2} |\chi_{\mathrm{S}_I}(r, \theta, t)|^2 \tag{B5}$$

which are, in turn, related to the time-dependent vibronic state of the system written in vector notation as

$$|\Psi(r, \theta, t)\rangle = \begin{pmatrix} \chi_{S_0}(r, \theta, t) \\ \chi_{S_1}(r, \theta, t) \\ \chi_{S_2}(r, \theta, t) \end{pmatrix} \tag{B6}$$

The trajectory-based (classical) electronic populations and nuclear kinetic energies are estimated as averages over the trajectories, namely as

$$O^{cl}(t) = \frac{1}{N_{traj}} \sum_{\alpha=1}^{N_{traj}} O^{\alpha}(t) \tag{B7}$$

where $O^{\alpha}(t) = |C^{\alpha}_{\mathrm{S}_I}(t)|^2$, $\frac{[P^{\alpha}_r(t)]^2}{2\mu_{\mathrm{OH}}}$, $\frac{[P^{\alpha}_{\theta}(t)]^2}{2I}$. In TSHED and in CTTSH, the electronic populations are estimated using the fraction of trajectories

$$\tilde{\rho}^{cI}_{\mathrm{S}_I}(t) = \frac{N_{\mathrm{S}_I}(t)}{N_{traj}} \tag{B8}$$

to distinguish it from Eq. (B7), where $N_{\mathrm{S}_I}(t)$ is the number of trajectories in state S_I at time t. In a surface-hopping scheme, internal consistency holds if $\tilde{\rho}^{cI}_{\mathrm{S}_I}(t) \simeq \rho^{cI}_{\mathrm{S}_I}(t)$ (with $\rho^{cI}_{\mathrm{S}_I}(t)$ the trajectory-averaged value of $|C^{\alpha}_{\mathrm{S}_I}(t)|^2$), and in general the "proper" quantities that should be compared to exact results is $\tilde{\rho}^{cI}_{\mathrm{S}_I}(t)$ from Eq. (B8). The dissociation probability is, instead, estimated by simply counting the number of trajectories that, at any time, are located at $r^{\alpha}(t) > r_{\mathrm{cutoff}}$ independently of the value $\theta^{\alpha}(t)$.

REFERENCES

[1]A. Abedi, N.T. Maitra and E.K.U. Gross, Phys. Rev. Lett. **105** (12), 123002 (2010).
[2]A. Abedi, N.T. Maitra and E.K.U. Gross, J. Chem. Phys. **137** (22), 22A530 (2012).
[3]G. Hunter, Int. J. Quantum Chem. **9**, 237–242 (1975).
[4]G. Hunter, Int. J. Quantum Chem. **9**, 311 (1975).
[5]G. Hunter, Int. J. Quantum Chem. **9**, 133 (1980).
[6]G. Hunter, Int. J. Quantum Chem. **19**, 755–761 (1981).
[7]N.I. Gidopoulos and E.K.U. Gross, arXiv:cond-mat/0502433 (2005).
[8]N.I. Gidopoulos and E.K.U. Gross, Phil. Trans. R. Soc. A **372**, 20130059 (2014).
[9]L.S. Cederbaum, J. Chem. Phys. **138** (22), 224110 (2013).
[10]Y.C. Chiang, S. Klaiman, F. Otto and L.S. Cederbaum, J. Chem. Phys. **140** (5), 054104 (2014).
[11]A. Abedi, F. Agostini, Y. Suzuki and E.K.U. Gross, Phys. Rev. Lett **110** (26), 263001 (2013).
[12]Y. Suzuki, A. Abedi, N.T. Maitra, K. Yamashita and E.K.U. Gross, Phys. Rev. A **89** (4), 040501(R) (2014).
[13]Y. Suzuki, A. Abedi, N.T. Maitra and E.K.U. Gross, Phys. Chem. Chem. Phys. **17**, 29271–29280 (2015).
[14]Y. Suzuki and K. Watanabe, Phys. Rev. A **94**, 032517 (2016).
[15]A. Schild and E.K.U. Gross, Phys. Rev. Lett. **118**, 163202 (2017).
[16]N.M. Hoffmann, H. Appel, A. Rubio and N. Maitra, Euro. Phys. J. B **91**, 180 (2018).
[17]A. Abedi, E. Khosravi and I. Tokatly, Euro. Phys. J. B **91**, 194 (2018).
[18]R. Requist and E.K.U. Gross, Phys. Rev. Lett. **117**, 193001 (2019).
[19]B.F.E. Curchod and F. Agostini, J. Phys. Chem. Lett. **8**, 831–837 (2017).
[20]L. Lacombe, N.M. Hoffmann and N.T. Maitra, Phys. Rev. Lett. **123**, 083201 (2019).
[21]F. Agostini, E.K.U. Gross and B.F.E. Curchod, Comput. Theo. Chem. **1151**, 99–106 (2019).
[22]P. Martinez, B. Rosenzweig, N.M. Hoffmann, L. Lacombe and N.T. Maitra, J. Chem. Phys. **154**, 014102 (2021).
[23]R. Requist, C. Li and E.K.U. Gross, Phil. Trans. R. Soc. A (2022).
[24]L.M. Ibele, B.F.E. Curchod and F. Agostini, J. Phys. Chem. A **126**, 12631281 (2022).

[25]F. Talotta, D. Lauvergnat and F. Agostini, J. Chem. Phys. **156**, 184104 (2022).
[26]L.M. Ibele, E.S. Gil, B.F.E. Curchod and F. Agostini, J. Phys. Chem. Lett. **14**, 11625–11631 (2023).
[27]E.V. Arribas, N.T. Maitra and F. Agostini, J. Chem. Phys. **160**, 054102 (2024).
[28]J. Kocák, E. Kraisler and A. Schild, J. Phys. Chem. Lett. **12**, 3204–3209 (2021).
[29]S. Giarrusso, P. Gori-Giorgi and F. Agostini, ChemRxiv (2024).
[30]S.K. Min, F. Agostini, I. Tavernelli and E.K.U. Gross, J. Phys. Chem. Lett. **8**, 3048–3055 (2017).
[31]A. Scherrer, F. Agostini, D. Sebastiani, E.K.U. Gross and R. Vuilleumier, Phys. Rev. X **7**, 031035 (2017).
[32]B.F.E. Curchod, F. Agostini and I. Tavernelli, Euro. Phys. J. B **91**, 168 (2018).
[33]J.K. Ha, I.S. Lee and S.K. Min, J. Phys. Chem. Lett. **9**, 1097–1104 (2018).
[34]E. Villaseco Arribas, F. Agostini and N.T. Maitra, Molecules **27**, 4002 (2022).
[35]P. Vindel-Zandbergen, S. Matsika and N.T. Maitra, J. Phys. Chem. Lett. **13**, 1785–1790 (2022).
[36]E. Marsili, M. Olivucci, D. Lauvergnat and F. Agostini, J. Chem Theory Comput. **16**, 6032–6048 (2020).
[37]F. Agostini and E.K.U. Gross, Eur. Phys. J. B **94**, 179 (2021).
[38]C. Pieroni, E.S. Gil, L.M. Ibele, M. Persico, G. Granucci and F. Agostini, J. Chem. Theory Comput. **20**, 580–596 (2024).
[39]P. Vindel-Zandbergen, L.M. Ibele, J.K. Ha, S.K. Min, B.F.E. Curchod and N.T. Maitra, J. Chem. Theory Comput. **17**, 3852–3862 (2021).
[40]M. Born and R. Oppenheimer, Ann. Phys. **84**, 457–484 (1927).
[41]G.H. Gossel, L. Lacombe and N.T. Maitra, J. Chem. Phys. **150**, 154112 (2019).
[42]F. Talotta, F. Agostini and G. Ciccotti, J. Phys. Chem. A **124**, 6764–6777 (2020).
[43]F. Agostini, I. Tavernelli and G. Ciccotti, Euro. Phys. J. B **91**, 139 (2018).
[44]R.E. Wyatt, Chem. Phys. Lett. **313** (1-2), 189–197 (1999).
[45]S.K. Min, F. Agostini and E.K.U. Gross, Phys. Rev. Lett. **115** (7), 073001 (2015).
[46]F. Agostini, S.K. Min, A. Abedi and E.K.U. Gross, J. Chem. Theory Comput. **12** (5), 2127–2143 (2016).
[47]C. Pieroni and F. Agostini, J. Chem. Theory Comput. **17**, 5969 (2021).
[48]L.M. Ibele, C. Pieroni, F. Talotta, B.F.E. Curchod, D. Lauvergnat and F. Agostini, in *Comprehensive Computational Chemistry (First Edition)*, edited by Manuel Yáñez and Russell J. Boyd, first edition ed. (Elsevier, Oxford, 2024), pp. 188–211.
[49]F. Talotta, S. Morisset, N. Rougeau, D. Lauvergnat and F. Agostini, Phys. Rev. Lett. **124**, 033001 (2020).
[50]F. Talotta, S. Morisset, N. Rougeau, D. Lauvergnat and F. Agostini, J. Chem Theory Comput. **16**, 4833–4848 (2020).
[51]E. Villaseco Arribas and N.T. Maitra, J. Chem. Phys. **158**, 161105 (2023).
[52]E. Villaseco Arribas, L.M. Ibele, D.L. abd N. T. Maitra and F. Agostini, J. Chem. Theory Comput. **19**, 7787–7800 (2023).
[53]E. Villaseco Arribas, P. Vindel-Zandbergen, S. Roya and N.T. Maitra, Phys. Chem. Chem. Phys. **25**, 26380–26395 (2023).
[54]J.C. Tully, Faraday Discuss. **110**, 407 (1998).

[55]J.C. Tully, J. Chem. Phys. **93**, 1061 (1990).
[56]M. Filatov, S.K. Min and K.S. Kim, Mol. Phys. **117**, 1128–1141 (2019).
[57]M. Filatov, S.K. Min and C.H. Choi, Phys. Chem. Chem. Phys. **21**, 2489–2498 (2019).
[58]I.S. Lee, J. Ha, D. Han, T.I. Kim, S.W. Moon and S.K. Min, J. Comput. Chem. **42**, 1755–1766 (2021).
[59]T.I. Kim, J.K. Ha and S.K. Min, Top. Curr. Chem. **380**, 1–27 (2022).
[60]A. Dines, M. Ellis and J. Blumberger, J. Chem. Phys. **159**, 234118 (2023).
[61]F. Agostini, E. Marsili, F. Talotta, C. Pieroni, E. Villaseco Arribas, L.M. Ibele and E. Sangiogo Gil, G-CTMQC accessed in July 2023, `https://gitlab.com/agostini.work/g-ctmqc`.
[62]Z. Lan, W. Domcke, V. Vallet, A.L. Sobolewski and S. Mahapatra, J. Chem. Phys. **122**, 224315 (2005).
[63]F.G. Eich and F. Agostini, J. Chem. Phys. **145**, 054110 (2016).
[64]F. Agostini, Euro. Phys. J. B **91**, 143 (2018).
[65]G. Granucci and M. Persico, J. Chem. Phys. **126**, 134114 (2007).
[66]G.M. Roberts, A.S. Chatterley, J.D. Young and V.G. Stavros, J. Phys. Chem. Lett. **3**, 348–352 (2012).
[67]C. Xie, J. Ma, X. Zhu, D.R. Yarkony, D. Xie and H. Guo, J. Am. Chem. Soc. **138**, 7828–7831 (2016).
[68]X. Xu, J. Zheng, K.R. Yang and D.G. Truhlar, J. Am. Chem. Soc. **136**, 16378–16386 (2014).
[69]M.L. Hause, Y.H. Yoon, A.S. Case and F.F. Crim, J. Chem. Phys. **128**, 104307 (2008).
[70]K. Rajak, A. Ghosh and S. Mahapatra, J. Chem. Phys. **148**, 054301 (2018).
[71]G. Christopoulou, T. Tran and G.A. Worth, Phys. Chem. Chem. Phys. **23**, 23684–23695 (2021).
[72]D. Lauvergnat, QuantumModelLib accessed in July 2023, `https://github.com/lauvergn/QuantumModelLib/tree/OOP{\_}branch`.
[73]D. Lauvergnat, ElVibRot-TnumTana Quantum Dynamics Code accessed in June 2023, `https://github.com/lauvergn/ElVibRot-TnumTan`.
[74]L. Dupuy, A. Rikus and N. Maitra, J. Phys. Chem. Lett. **15**, 2643–2649 (2024).
[75]M.J. Frisch, G.W. Trucks, H.B. Schlegel, G.E. Scuseria, M.A. Robb, J.R. Cheeseman, G. Scalmani, V. Barone, G.A. Petersson, H. Nakatsuji, X. Li, M. Caricato, A.V. Marenich, J. Bloino, B.G. Janesko, R. Gomperts, B. Mennucci, H.P. Hratchian, J.V. Ortiz, A.F. Izmaylov, J.L. Sonnenberg, D. Williams-Young, F. Ding, F. Lipparini, F. Egidi, J. Goings, B. Peng, A. Petrone, T. Henderson, D. Ranasinghe, V.G. Zakrzewski, J. Gao, N. Rega, G. Zheng, W. Liang, M. Hada, M. Ehara, K. Toyota, R. Fukuda, J. Hasegawa, M. Ishida, T. Nakajima, Y. Honda, O. Kitao, H. Nakai, T. Vreven, K. Throssell, J.A. Montgomery, Jr., J.E. Peralta, F. Ogliaro, M.J. Bearpark, J.J. Heyd, E.N. Brothers, K.N. Kudin, V.N. Staroverov, T.A. Keith, R. Kobayashi, J. Normand, K. Raghavachari, A.P. Rendell, J.C. Burant, S.S. Iyengar, J. Tomasi, M. Cossi, J.M. Millam, M. Klene, C. Adamo, R. Cammi, J.W. Ochterski, R.L. Martin, K. Morokuma, O. Farkas, J.B. Foresman and D.J. Fox, Gaussian16 Revision C.01 2016, Gaussian Inc. Wallingford CT.
[76]T.J. Park and J.C. Light, J. Chem. Phys. **85**, 5870–5876 (1986).
[77]C. Leforestier, R.H. Bisseling, C. Cerjan, M.D. Feit, R. Friesner, A. Guldberg, A. Ham-

merich, G. Jolicard, W. Karrlein, H.D. Meyer, N. Lipkin, O. Roncero and R. Kosloff, J. Comp. Phys. **94**, 59–80 (1991).